Structure–Property Relationships of a New Series of Segmented Polyether–Polyester Copolymers

P. C. MODY* and G. L. WILKES,† *Chemical Engineering Department, Virginia Polytechnic Institute and State University, Blacksburg, Virginia 24061* and K. B. WAGENER, *American Enka Research, Akzona Inc., Enka, North Carolina 28728*

Synopsis

The work reported focuses on the structure–property relationships of a new series of segmented polyether–polyester copolymers. Poly(ethylene oxide-hydantoin) is the soft segment, while poly(tetramethylene terephthalate) is the hard block and is suceptible to crystallization. The structure–property relationships have been addressed under three different subdivisions: (1) mechanical properties, (2) orientation effects and phase separation, and (3) morphology and superstructure. Where possible, a correlation has been made between these three categories.

INTRODUCTION

In recent years, the commercialization of thermoplastic elastomers has stimulated interest in synthesizing and studying the behavior of new and related materials. Characteristically, thermoplastic elastomers are copolymers consisting of two types of blocks—one being amorphous with a T_g below the use temperature, the second block being either glassy or semicrystalline (at the use temperature) and serving as an "anchor" for the soft blocks. Compatability of the two segments also strongly influences the final properties. The intermolecular association of the hard blocks can be incorporated into the molecular structure in a number of ways. A well-known mechanism of intermolecular association is through the formation of a separate glassy phase with a continuous elastomeric matrix, as in many of the SBS block copolymers. Crystallization of the hard segments provides another mechanism of intermolecular association, as in the poly(tetramethylene terephthalate)–poly(tetramethylene ether) segmented copolymers, an example being the Hytrel materials.[1–3] The good performance of these latter systems has stimulated research directed toward the understanding of their structure–property relationships as well as promoting other economical synthetic routes for preparing related polyester–polyether segmented copolymers.

The final morphology of the solid depends on several factors, such as the nature and concentration of the crystallizable components and the method of film preparation (solvent used, thermal history, composition ratio, etc.). Regarding superstructure in segmented copolymers, Wilkes and Samuels[4] were the first to report the occurrence of a elastomeric fringe micellar spherulitic morphology for a select series of segmented urethanes cast from chloroform, whereas a similar

* Present address: American Enka Research, Akzona Inc., Enka, NC 28728.
† To whom correspondence should be sent.

Journal of Applied Polymer Science, Vol. 26, 2853–2878 (1981)
 CCC 0021-8995/81/092853-26$02.60

series investigated by Cooper et al.[5] showed no superstructure when using methylene chloride as the casting solvent. Spherulitic textures have since been observed in other segmented polyurethanes–ureas,[6] whereas the more conventional chain-folded lamellae-type spherulites have been observed in the segmented polyester–polyether thermoplastic elastomers.[3,7–10]

Work carried out by Cooper et al.[3] on the commercial segmented polyether–polyester systems known as the Hytrel materials have shown four types of superstructure. Types I, II, and III are spherulitic (with the major optical axis at an angle of 45, 90, and 0° to the radial direction, respectively). The fourth type is one in which no anisotropic spherulitic structure was reported to exist. These different morphologies were obtained by varying the sample preparation method. A schematic depicting the above basic spherulitic models is shown in Figure 1. Stress–strain measurements on these same samples indicate that the stress past the yield point increases in the order of texture III, "no texture," texture I, and texture II. Infrared dichroism results have shown that the extent of hard-segment orientability increases in the opposite order—II, I, "no texture," and III. These data suggest that the greater the ability of hard segments to resist orientation in the stretch direction, the higher is the stress level.

The dynamic-mechanical spectra of this same series revealed only one T_g and one T_m associated with the soft and hard segments, respectively. The magnitude of both transition temperatures shifts progressively to a higher temperature with increasing hard-segment content. Interestingly, the Gorden–Taylor equation was found to accurately model the T_g behavior of these samples, provided that the crystalline polyester component was not included in the definition of the hard-segment calculation. Thus, the authors thereby suggested that the uncrystallized (amorphous) hard segments in these materials form a relatively compatible interlamellar amorphous phase with the polyether component.

The work reported here concerns studies on the structure–property relationships of a new series of poly(ethylene oxide–hydantoin) and poly(tetra-

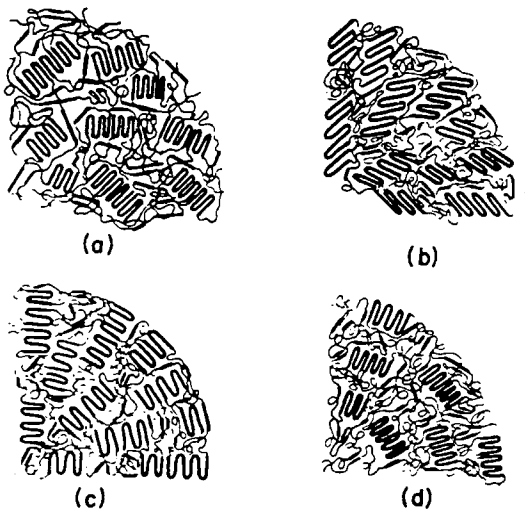

Fig. 1. Quadrants of schematic spherulite models showing different types of morphologies. After Cooper.[3]

methylene terephthalate) segmented copolymers. Poly(ethylene oxide–hydantoin) is the soft segment, while poly(tetramethylene terephthalate) is the hard block and is susceptible to crystallization. As expected, similarity between this series and the Hytrel copolymers exists, as will become evident from the data now presented.

EXPERIMENTAL

Materials

The series of polymers discussed were synthesized by a step-polymerization, condensation-type reaction between dimethyl terephthalate, butanediol, and a hydroxy-terminated polyether, 5,5-dimethyl-1,3-poly(oxyethylene)hydantoin. Mole percentages of the reactants present in the segmented copolyester were confirmed by C, H, and N analysis and by 60-MHz NMR. The unique polyether used in the synthesis is prepared by first adding 2 mol ethylene oxide to 5,5-dimethyl-1,3-hydantoin, followed by the desired degree of base-catalyzed ethoxylation. The hydantoin unit appears in the center of the soft-segment block and serves to inhibit crystallization of poly(oxyethylene) via depression of its melting point below room temperature (see Fig. 2). The number-average molecular weight of the modified poly(oxyethylene) segment is 1200, while the number-average molecular weight of the hard segment varies from 900 to 1400 depending upon the composition of the polymer. Three different compositions of the polymer were prepared, namely, 60-H/40-S, 50-H/50-S, and 40-H/60-S, where the first number denotes the weight percentage of the hard segment and the second number identifies the weight percentage of the soft segment.

Solution-cast films were prepared from a 6% solution of the polymer in chloroform on a Teflon surface at room temperature (~23°C) and 58°C in an temperature-controlled oven. The conditions for casting films, i.e., temperature of casting, rate of evaporation, and solution concentration, were kept quite uniform throughout the study. All films were further vacuum dried for at least 24 h prior to any tests. Portions of the films cast at room temperature were annealed at 60 and 120°C for 1 h. Some of those cast at 58°C were also annealed at 120°C for 1 h. Some additional films were compression molded at 215 to 230°C (depending on the composition of the polymer) between Teflon surfaces. The dry polymer (crumb form) was first heated at the desired temperature for about 5 min and then compressed to 15,000 psi. The films were then quenched in 20°C water. After the films were prepared, they were stored until tested in a vacuum desiccator.

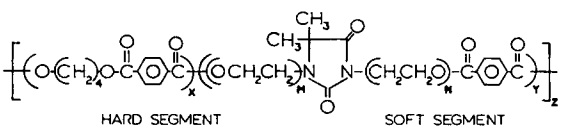

Fig. 2. Chemical structure of the copolymer series studied.

Methods

Mechanical Methods

A VTM-II Tensilon (Toyo Measuring Instrument Co.) was used to measure the stress–strain behavior. Measurements were made at room temperature, and a crosshead speed of 40 mm/min was used in all cases. All calculations of the stress were based on the initial cross-sectional area which provide the engineering stress. Some selected samples were subjected to cyclic deformation. Also, stress relaxation experiments were carried on some selected samples at ambient conditions.

Dynamic-mechanical measurements were carried out on a Rheovibron Viscoelastomer (Toyo Baldwin Co. Ltd.) A frequency of 3.5 Hz was employed for all mechanical spectra.

Optical Methods

The birefringence–strain behavior was measured by a Babinet compensator technique as described elsewhere.[11] Linear infrared dichroism measurements were carried out on a Digitalab FTIR system. Very thin films (of the order of 1.0 to 1.5 mil) of the 60-H/40-S, 50-H/50-S, and 40-H/60-S polymers were cast from chloroform at room temperature. Three samples of each of these polymers were taken and stretched to 50, 100, and 200% elongation, respectively, and clamped. Absorption spectra of these systems were measured with the polarization vector parallel ($A_{\parallel}$) and perpendicular ($A_{\perp}$) to the principal deformation axis. Also absorption spectra of pure poly(ethylene oxide), cast from chloroform, and pure poly(butylene terephthalate) films, pressed at 250°C, were obtained. In addition, the dichroic ratio D was determined. This parameter is defined as the absorption measured parallel with polarization ($A_{\parallel}$) to the deformation axis divided by the absorption measured with perpendicular polarization ($A_{\perp}$) to the same axis.

A Phillips table-top x-ray generator PW 1720 was used to obtain wide-angle x-ray diffraction patterns. Samples were about 10–12 mil thick, and the exposure time was of the order of 8 h per sample. The operating voltage was 40 kV and the current, 25 mA.

Small-angle x-ray scattering studies were carried out using an automated Kratky camera described elsewhere.[12]

A scanning electron microscope Super III-A (ISI) was used for morphological investigations. The samples were placed on stubs and sputter coated with gold, giving a conductive thickness of approximately 50–75 Å.

Small-angle light scattering experiments were also performed on these samples to learn about the superstructure and its deformation. In order to study the deformation behavior of spherulites, the sample was clamped on a stretcher device such that the length-to-width ratio was greater than 3 in order that the deformation be unidirectional. The sample was placed in the path of a linearly polarized laser beam of wavelength 6320 Å. The scattered light which passed through an analyzer was recorded on a photographic film. Also, computer programs were written so as to obtain light scattering patterns from theoretical models. Comparisons of these theoretical patterns were then made with experimental observations.

RESULTS AND DISCUSSION

In order to make a systematic analysis of the structure–property relationships of these polymers, it will be useful to discuss the results under the three subdivisions of: (1) mechanical properties, (2) orientation effects and phase separation, and (3) morphology and superstructure. When possible, correlations between these subdivisions will be made.

Mechanical Properties

The dynamic-mechanical curves values of E' and E'' vs. temperature plots for the 40-H/60-S (dotted lines) and the 60-H/40-S (solid lines) cast at room temperature are shown in Figure 3. As expected, a distinct T_g (β relaxation) is noted at about -40 and $-44°C$, respectively. It is of interest to note that Cooper et al.[3] observed that the soft-segment T_g of the Hytrel materials shifted toward its homopolymer values with an increase in soft-segment content. This shift toward the homopolymer value with an increase in soft-segment content is probably due to the fact that there is a higher degree of mixing between the segments in the Hytrel systems. This increasing trend is not observed in our data and presumably is due to the fact that there is better phase separation in our materials. Differences in modulus behavior below the soft-segment T_g are not deemed significant in view of the flucuation on the original raw data points (not shown). The temperature dependence of E' above the soft-segment T_g illustrates the reinforcing effect of the PBT hard block. With increasing PBT content, the soft-segment glass transition becomes somewhat less, while E' above T_g is significantly higher. This trend is expected, since the increase in PBT content results in a longer average hard-block length and a greater degree of crystallinity.

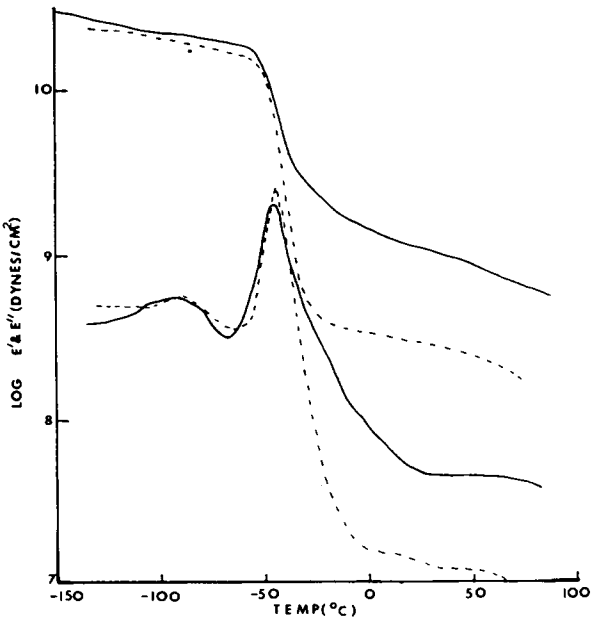

Fig. 3. Dynamic-mechanical spectra for the 40-H/60-S and 60-H/40-S materials cast at room temperature: E' and E'' vs. temperature.

The effect of annealing the 40-H/60-S sample on the moduli curves is shown in Figure 4. In this figure, the dotted lines represent the room-cast material, while the solid line represents the annealed samples. On annealing the samples, one tends to promote further hard-segment crystallinity and, consequently, there is an increase in the modulus above the T_g of the soft segment. The 60-H/40-S material on annealing (figure not shown) shows similar behavior. The difference in moduli curves for the pressed-quenched (solid lines) and room-cast (dotted lines) samples of the 60-H/40-S material is shown in Figure 5. On rapidly quenching the molded polymer, the degree of domain formation apparently decreases. This causes more mixing between the hard and soft segments. This speculation will be directly supported at a later stage by small-angle x-ray scattering data on these systems. The T_g of the soft segment for the pressed-quenched material is −36°C, which is 8°C higher than the T_g of the room-cast material. Due to a lower percentage of hard-segment content present in the 40-H/60-S material, the shift is not so pronounced in this material (data not shown).

As seen in Figures 3, 4, and 5, there is also a lower temperature loss peak around −85°C involving secondary local mode motion (γ relaxation). This is apparently associated with the amorphous component of the hard segment. Previous work carried out on pure PBT by Ward and co-workers[13] shows a γ relaxation at −65°C (412 Hz). Illers and Brown[14] attributed this relaxation to a combination of molecular motions. One is the crank shaft-type motion of the methylene sequences, and the other is local mode of the chain segments containing the

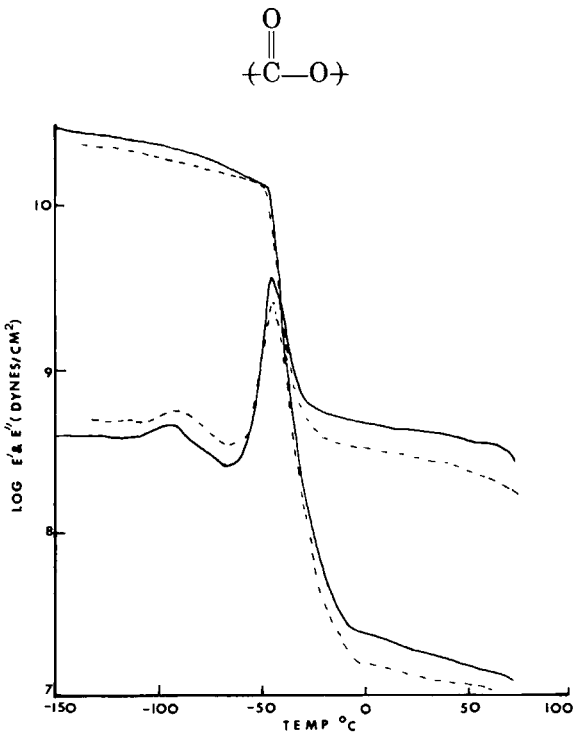

Fig. 4. Dynamic-mechanical spectra for the 40-H/60-S material cast at room temperature and room-cast annealed at 120°C: E' and E'' vs. temperature.

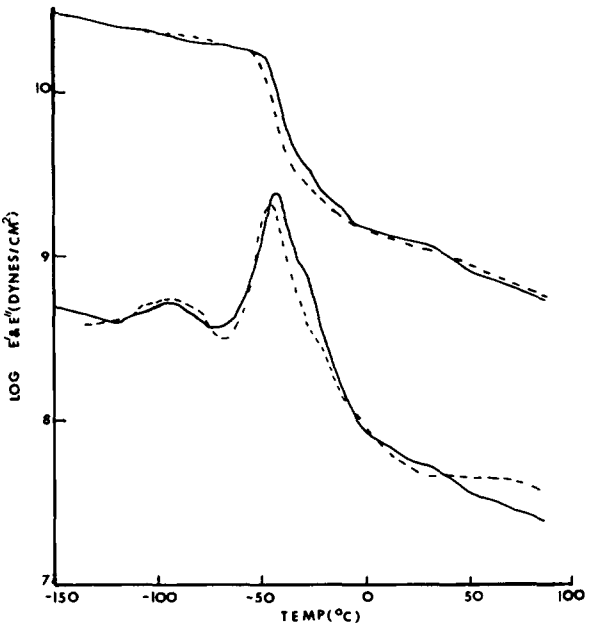

Fig. 5. Dynamic-mechanical spectra for the 60-H/40-S material cast at room temperature and room-cast annealed at 120°C: E' and E'' vs. temperature.

groups in the main chain. It should be borne in mind that the frequency at which our measurements were made was 3.5 HZ and that the temperature at which the peak appears is dependent on operational frequency. It is on this basis we can rationalize an upward shift, although an increase of nearly 20°C seems somewhat high. In Figure 4, the secondary loss peak (γ transition), which is dependent on the amorphous PBT, has a slightly lower value in the case of the annealed 40-H/60-S material likely due to an increase in PBT crystallinity.

The stress–strain behavior is in keeping with the dynamic-mechanical spectra. Figure 6 shows the stress vs. percent elongation curves for the 40-H/60-S, 50-H/50-S, and 60-H/40-S samples cast at room temperature. As expected, with an increase in the hard-segment content concentration, the stress for a particular strain increases. Increasing the hard-segment content results in a higher modulus and a lower ultimate elongation. The increase in modulus with an increase in hard-segment content was as noted in the dynamic-mechanical spectra of these polymers.

Figure 7 shows the stress vs. percent elongation curves for the 40-H/60-S material subjected to different thermal history and preparation conditions. On annealing, increased crystallization and perfection of the PBT crystallites occurs thereby increasing the stress behavior. In Figure 7, it is noted that the 40-H/60-S pressed-quenched samples has an intermediate value of stress until about 450% elongation, after which there is a sudden increase in the stress. One basis on which one might rationalize these data is that some degree of strain-induced crystallization phenomena may be taking place for this initially lower crystallinity material; however, this is only speculation. The 60-H/40-S material shows similar behavior (data not shown).

Some selected samples were subjected to cyclic tensile deformation. A plot

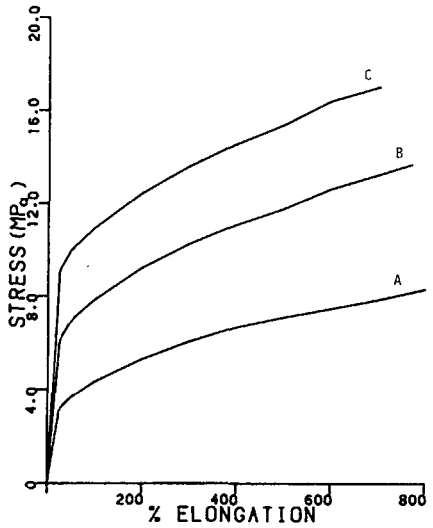

Fig. 6. Stress vs. percent elongation curves for the (A) 40-H/60/S, (B) 50-H/50-S, and (C) 60-H/40-S materials cast at room temperature.

of percent hysteresis (defined as the area under the loading–unloading curve divided by the area under the total loading curve[15]) vs. percent elongation for the three room-cast samples is shown in Figure 8(a). As expected, higher hard-segment content results in higher hysteresis because of greater crystallinity and plastic deformation within this phase. Thus, in order to disrupt the continuity of the additional crystallites formed due to annealing, a higher value of stress is required. Very strikingly, at approximately 120% elongation, the connectivity of the hard-segment material appears to become discontinuous and

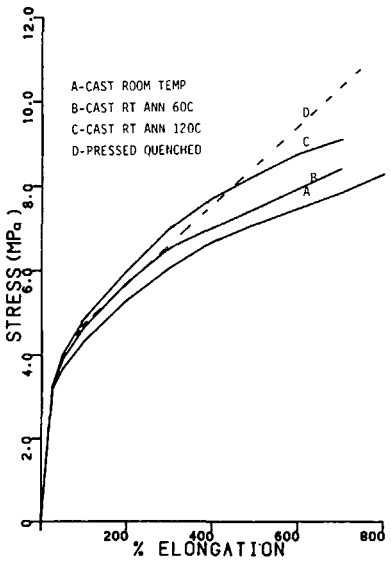

Fig. 7. Stress vs. percent elongation curves for the 40-H/60-S material subjected to different thermal and preparation conditions.

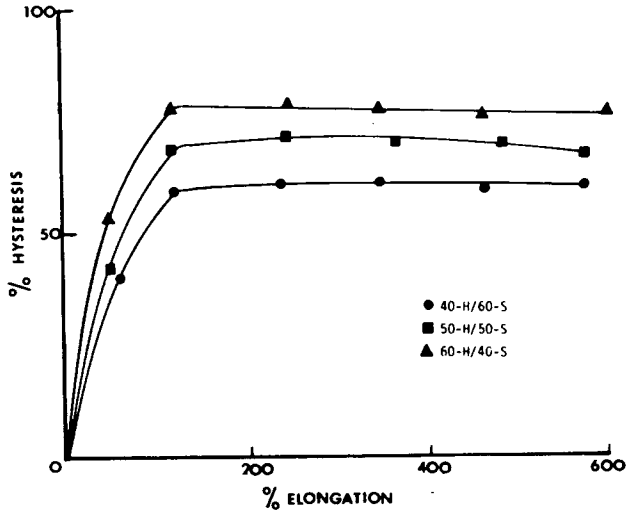

(a)

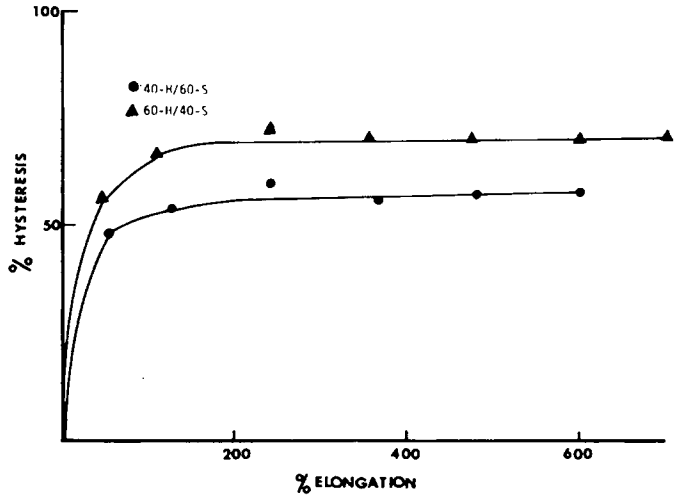

(b)

Fig. 8. Plots of percent hysteresis vs. percent elongation for the (a) cast films (b) pressed quenched films.

there is no further increase in percent hysteresis. Figure 8(b) shows a plot of percent hysteresis vs. percent elongation for the 40-H/60-S and 60-H/40-S pressed-quenched samples. An important observation is that the limiting value of percent hysteresis reached is greater in the room-cast sample when compared with the pressed-quenched material. Due to better mixing between the hard and soft segments in the pressed-quenched films, as suggested by the dynamic-mechanical data (and later by the SAXS data), the phase separation and crystallinity are less when compared to those of the room-cast sample. As might be expected for this type of deformation, this texture leads to a greater recoverability in stress and consequently a lower value of hysteresis.

Orientation Effects and Phase Separation

In order to obtain an index of orientation behavior of these polymers, the techniques of linear birefringence and linear dichroism were employed. A plot of birefringence (Δ) vs. extension ratio (λ) for the 40-H/60-S, 50-H/50-S, and 60-H/40-S samples (Fig. 9) clearly shows that the birefringence for a fixed extension ratio is higher with an increase in hard-segment content. This is expected due to the higher crystallinity and associated orientation of the PBT crystals. Due to the aromatic nature of PBT, one expects that the intrinsic birefringence for the PBT segment is greater than the intrinsic birefringence for the poly(ethylene oxide–hydantoin) segment. This suggests that much of the birefringence contribution is primarily due to the hard segment. This speculation will be indirectly supported by the dichroism data which show, within experimental limitations, that the major orientation arises from the PBT phase while the poly(ethylene oxide)hydantoin chains display little orientation. Figure 10 shows a plot of birefringence vs. extension ratio (λ) for the 50-H/50-S sample cast at room temperature for both extension and retraction. The birefringence value is higher in the retraction case as compared to the extension experiment for the same extension ratio. The higher value in the retraction experiment is due to the limited disorientation of the hard crystallites, which contribute greatly to the birefringence. In brief, the soft segment nearly disorients when the strain is removed, whereas the hard segment remains partially oriented.

Since the orientation–disorientation process of the PBT crystals is not instantaneous, the birefringence for these systems for a fixed elongation was measured as a function of time. Figure 11 shows the birefringence vs. time behavior of the 50-H/50-S and 60-S/40-S copolymers cast at room temperature for

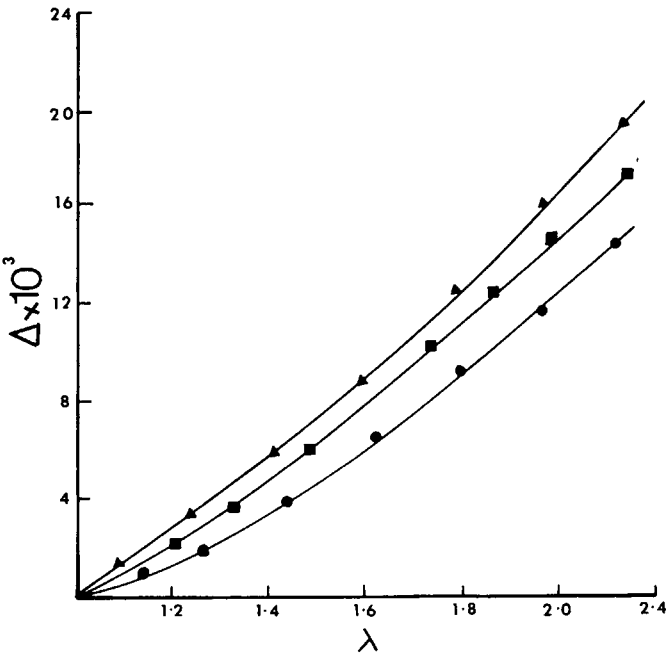

Fig. 9. Plot of birefringence vs. extension ratio for the (●) 40-H/60-S, (■) 50-H/50-S, and (▲) 60-H/40-S materials cast at room temperature.

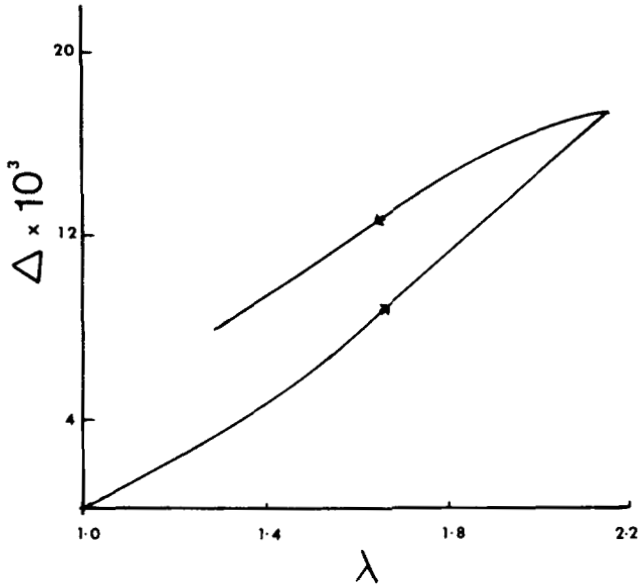

Fig. 10. Plots showing birefringence vs. extension ratio for an extension-retraction experiment for the 50-H/50-S system.

an extension ratio of 1.8. As time progresses, the PBT crystals orient in the stretch direction, and this leads to an increase in birefringence with time. As observed earlier, stress decreased with time at a fixed elongation. Thus, the stress-optical coefficient (SOC), which is defined as the ratio of birefringence to true stress for a fixed strain, increases with time apparently due to the time

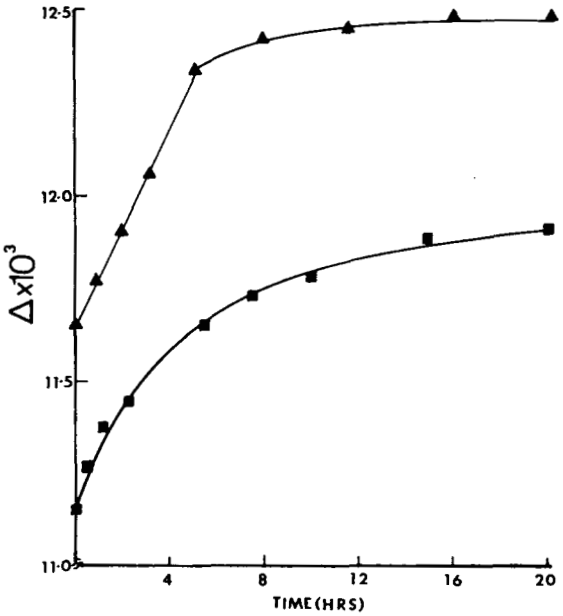

Fig. 11. Plot of birefringence vs. time for the (■) 50-H/50-S and (▲) 60-H/40-S materials cast at room temperature for an extension ratio of 1.8.

dependent orientation of the PBT phase. This is contrary to the behavior one would obtain from a good crosslinked elastomeric material such as *cis*-1,4-polybutadiene. For an ideal elastomer, the SOC would remain constant with time. Our data thus show deviation from classical rubber elasticity theory,[16] as was initially expected based on the nature of these semicrystalline segmented materials.

Dichroism measurements made on some selected samples clearly indicate that the orientation effect is primarily due to the PBT segment, confirming the

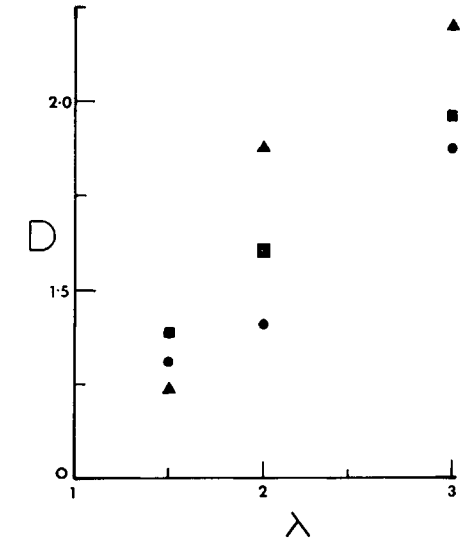

(a)

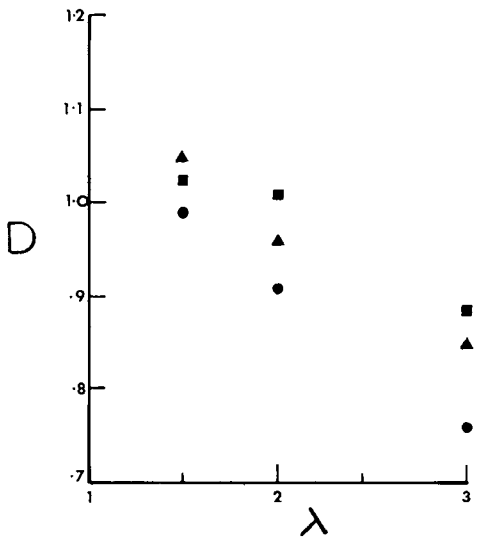

(b)

Fig. 12. (a) Plot of dichroic ratio vs. extension ratio for the 497 cm^{-1} band. (b) Plot of dichroic ratio vs. extension ratio for the 872 cm^{-1} band. (c) Plot of dichroic ratio vs. extension ratio for the 1504 cm^{-1} band. Cast room temperature, (●) 40-H/60-S, (■) 50-H/50-S, (▲) 60-H/40-S.

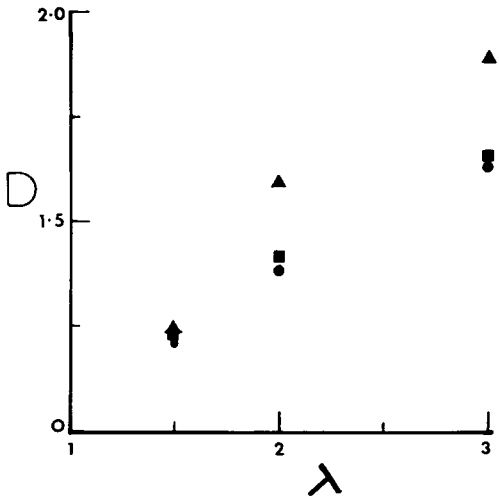

(c)

Fig. 12. (*Continued from previous page.*)

speculation made earlier. Plots of the dichroic ratio ($D = A_{\parallel}/A_{\perp}$) vs. extension ratio ($\lambda$) for the three polymers, namely, 40-H/60-S, 50-H/50-S, and 60-H/40-S, cast at room temperature are shown in Figures 12(a), 12(b), and 12(c) for the frequencies 497, 872, and 1504 cm^{-1}, respectively. It is noted that the dichroic ratio increases with an increase in percent elongation for each of the three polymers for the 497 and 1504 cm^{-1} bands. Due to the nature of the transition moment of the 872 cm^{-1} band, the associated dichroism shows a decreasing trend with elongation. Although it is known that the dichroism reported here arises from the PBT segment, it is uncertain whether the dichroism is due strictly to the crystalline region, the amorphous region, or both. Infrared studies on PBT[17–19] indicate that the peaks in the absorbance spectra for the 1504, 875, and 502 cm^{-1} bands arise due to the benzene ring breathing mode of PBT, the out-of-plane bending mode of the benzene ring of PBT, and the in-plane wagging motion of the C=O, respectively.

The same assignments can be extended to the systems under study, since they have PBT as one of its components and it is this component which shows dichroism. The transition moment angle, α, the angle which the transition moment makes with the chain axis, is not precisely known for these frequencies, although the limiting value of this angle can reasonably be assumed to calculate the Hermans' orientation function for this segment. For the 497 and 1504 cm^{-1} bands where the motion is along the chain, a value of $\alpha = 0$ is assumed. Thus, f_i, the hypothetical orientation function, can be calculated. Figures 13(a) and 13(b) show plots of the hypothetical Hermans' orientation function for the PBT segment vs. extension ratio for the 497 and the 1504 cm^{-1} bands, respectively. As expected, with an increase in extension ratio, the orientation function (hypothetical) increases; but the latter, within experimental limitations, does not show a definite trend with respect to an increase in hard-segment content. It is noted that in both adsorption bands the upper value of f approaches 0.3, which is not particularly high. It should be stated that no significant dichroism was

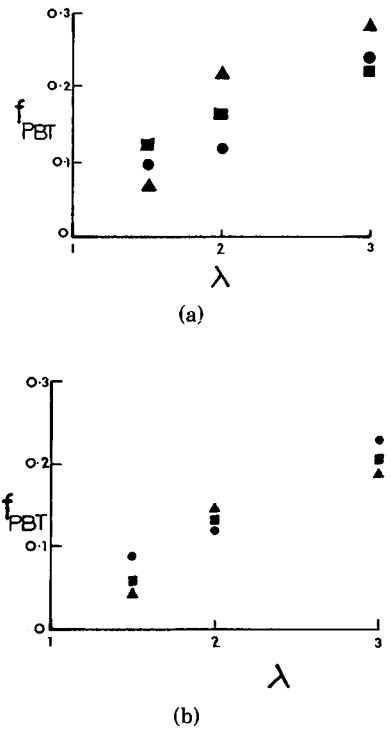

Fig. 13. Plots of hypothetical Hermans' orientation function vs. extension ratio for the (a) 497 cm^{-1} and (b) 1504 cm^{-1} absorption bands. Cast room temperature, (●) 40-H/60-S, (■) 50-H/50-S, (▲) 60-H/40-S.

observed in any of the absorption bands associated with the soft segment. While it is expected that some orientation of this phase would occur, particularly during the initial deformation, apparently it is not large and possibly decreases by relaxation soon after the deformation occurs.

It was speculated earlier that the annealed samples have the greatest degree of phase separation when compared with the room-cast and pressed-quenched samples, the latter being the least phase-separated. Some qualitative small-angle x-ray scattering experiments support this speculation. Figure 14 shows smeared plots of scattered intensity, $I(\theta)$, vs. scattering angle for the 40-H/60-S materials having different annealing and preparation conditions. The invariant of the electron density, Q, which is proportional to the degree of phase separation, is expressed as

$$Q = \int_{\theta} I(\theta)\, \theta d\theta$$

where $I(\theta)$ is the smeared intensity and θ is the scattering angle. Due to the similar nature of the tail region in these curves, the invariant can be approximated by the area under the curve. Thus, it can be inferred that the degree of phase separation increases upon annealing as might be expected. Although the data are smeared, it still is obvious that the shoulder positions of the scattering angle decreases to lower values on annealing and are the highest for the pressed-quenched material. Consequently, there is an increase in the d, or long, spacing.

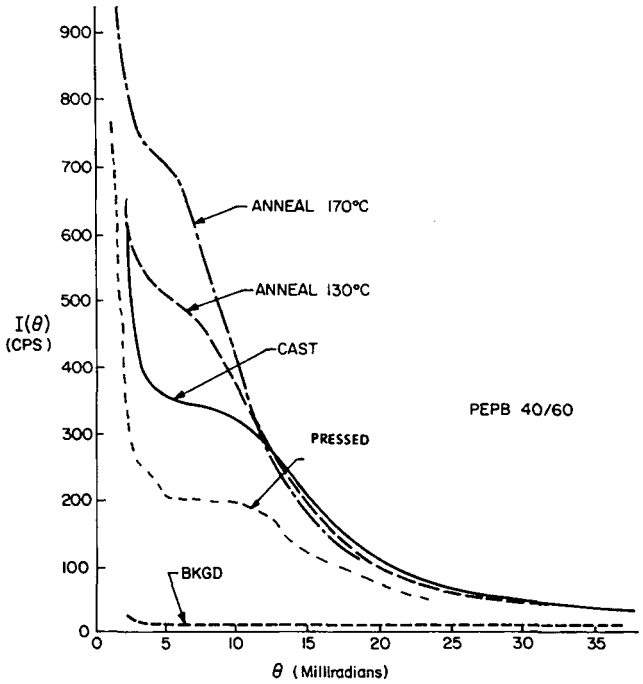

Fig. 14. Plot of small-angle x-ray scattered intensity vs. scattering angle for the 40-H/60-S material for different annealing and preparation conditions.

This is believed due to the thickening of the PBT crystals upon annealing and is expected. While the data are not shown, similar SAXS behavior and their interpretation followed for the 60-H/40-S sample.

Morphology and Superstructure

In order to study the superstructure formed within these polymers, scanning electron microscopy as well as small-angle light scattering experiments were performed. Figure 15 is a scanning electron micrograph of the 40-H/60-S sample annealed at 120°C. The superstructure observed is clearly spherulitic in nature, although the texture is not as distinct as has been noted in solution cast films of some other crystallizable segmented polymers.[20] The deformation of these spherulites is reasonably uniform in nature, and the spherulites tend to display ellipsoidal shape. Small-angle light scattering experiments confirm this observation, as will be pointed out shortly.

In order to examine the anisotropy of the superstructure formed, small-angle light scattering experiments were performed. Different light scattering patterns were obtained for different sample preparation conditions (Figs. 16, 17, and 18), and all these patterns suggest spherulitic structures similar to those proposed for the Hytrel materials by Cooper et al.[3] Specifically, these consist of PBT radial lamellae with interradial amorphous regions which are a mixture of poly(ethylene oxide–hydantoin) soft segments and uncrystallized PBT hard segments. Figure 16 shows the H_v scattering patterns, which are four-leaf clover patterns, as a function of deformation for the 40-H/60-S pressed-quenched sample. These results indicate that the spherulitic morphology is the so-called

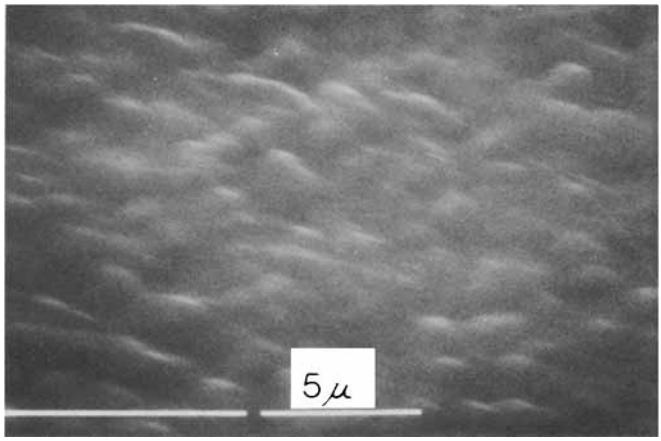

Fig. 15. Scanning electron micrograph of room-cast 120°C-annealed samples of 40-H/60-S.

usual ±45° spherulite with the principal polarizability of the lamellae either parallel or perpendicular to the radial direction [Figs. 1(c) and 1(d)]. On the contrary, a 0–90° four-leaf clover pattern is obtained from a solution-cast 40-

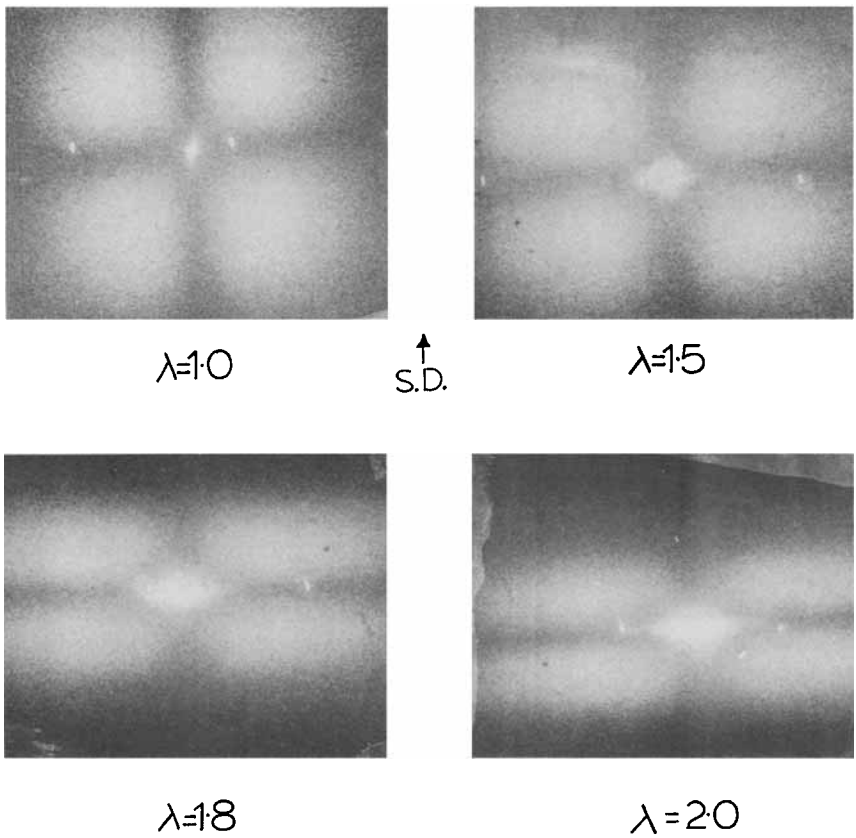

Fig. 16. H_v SALS patterns as a function of deformation for the 40-H/60-S pressed-quenched sample.

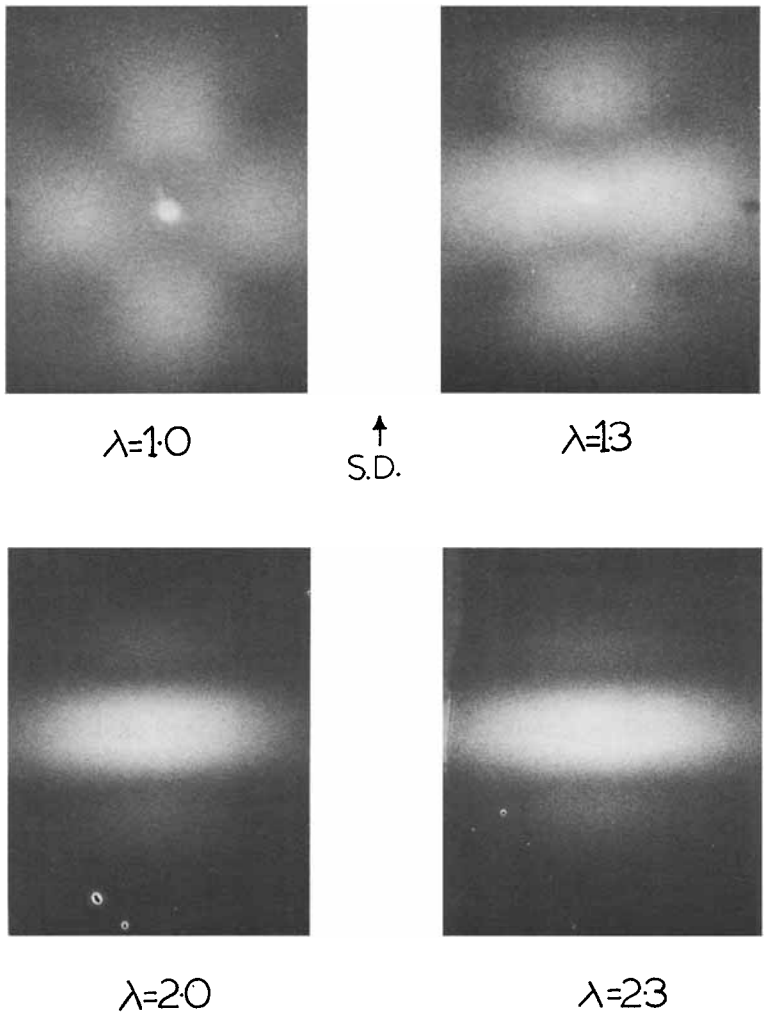

Fig. 17. H_v SALS patterns as a function of deformation for the 40-H/60-S material cast at room temperature and annealed at 120°C.

H/60-S material followed by annealing at 120°C (Fig. 17). The spherulitic texture of the so-called unusual 0–90° spherulites can be accounted for if one assumes that the principal polarizability of the lamella are at an angle of 45° to the spherulitic radius [Figs. 1(a) and 1(b)]. A more diffuse eight-lobe pattern is obtained for the 50-H/50-S polymer cast at room temperature and annealed at 120°C (Fig. 18). The latter apparently is a hybrid morphology between the ±45 and the 0–90° patterns. The 0–90° and the hybrid morphologies were not easily reproducible. Film preparation under seemingly identical conditions did not always give the same superstructure. Unfortunately, due to lack of reproducible results, no correlation could be positively made with the associated mechanical properties.

One of the ways in which the scattered behavior can be analyzed is by the "model approach." This method requires one to formulate a molecular model for the scattering system in question, calculate its scattering behavior, and then

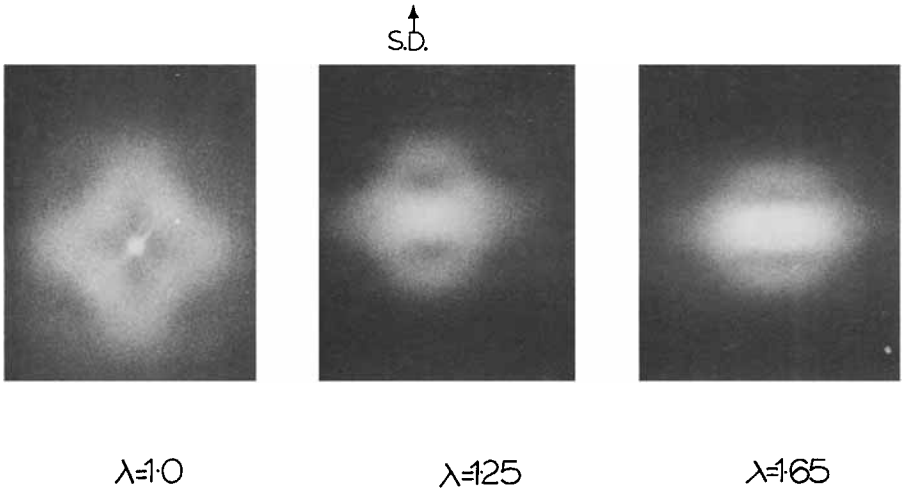

Fig. 18. H_v SALS patterns as a function of deformation for the 50-H/50-S material cast at room temperature and annealed at 120°C.

compare this with the observed behavior from the experimental system. To do this, one generally calculates the scattering intensity of the model by the "summation of amplitudes."

A number of models that enable one to predict the pattern exist. One of these has been proposed by Samuels[21] and it is a three-dimensional approach. A second has been proposed by Stein-Clough-Van Aartsen (SCV),[22] the latter being a two-dimensional approach. The difference is that upon deformation, the high-intensity regions move to lower radial scattering angles, while the lower-intensity contour lines stay elongated to a higher radial angle for Samuels' model (Fig. 19), whereas the opposite takes place in the SCV model (Fig. 20). The equations used to calculate the theoretical patterns for both these models are given in the Appendix.

In order to obtain the ±45° four-clover leaf pattern for Samuels' model, β = 0 in the equations given in the Appendix. Predictions for this case have been made by Samuels.[20] When the polarizability of the lamellae is inclined at 45° or the molecular chains are tilted at 45° to the lamella surface, the lamella principal axis being in the radial direction, $\beta = 45°$. The final intensity is obtained by adding intensities obtained from eq. (1) (Appendix) by putting $\beta = -45°$. Patterns for this case as a function of deformation are shown in Figure 21 for extension ratios of 1.0, 1.5, 2.0, and 3.0. These theoretical contour plots indicate that the lobes at the poles come toward the equator with an increase in extension ratio. This is in keeping with experimental results (Fig. 17).

For the SCV model, β being equal to 45°, a 0–90° pattern (for no deformation) identical to experimental results is obtained, Figure 22(a). Using the SCV model and $\beta = 45°$, deformations of 20 and 50% the calculated patterns obtained [Figs. 22(b) and 22(c)] are *not similar* to that obtained from experimental results. Thus, it is observed that the patterns obtained by Samuels' model for the 0–90° spherulites as a function of deformation are more in keeping with experimental observation. On the other hand, the SCV model gives patterns that are not similar to those obtained experimentally. This may be due to the following reason. The SCV model is based on the bessel function approach; and due to

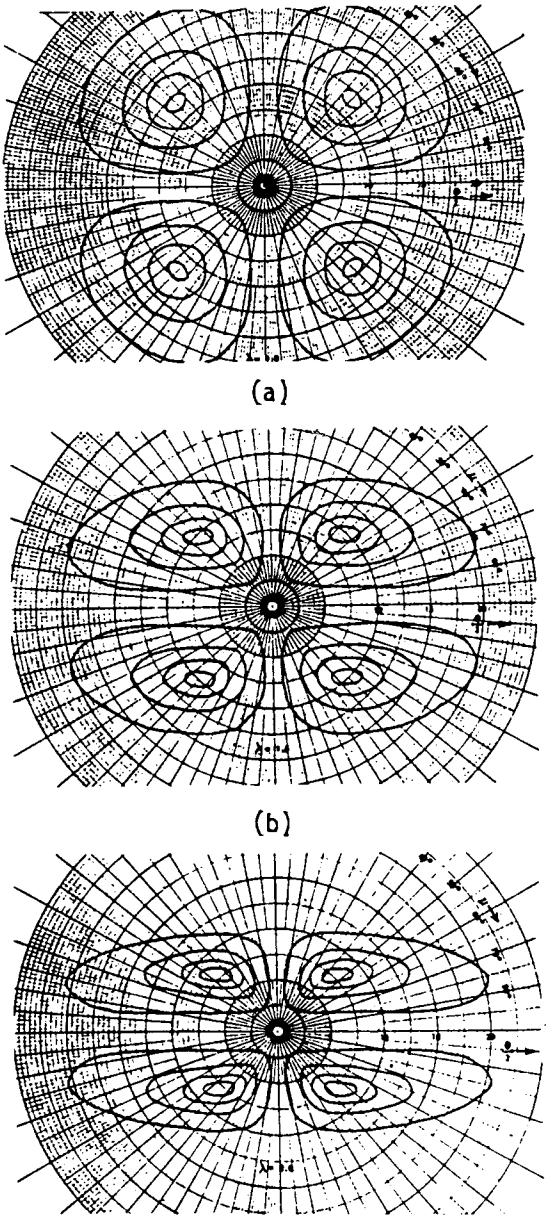

Fig. 19. Theoretically predicted changes in the H_v SALS patterns using Samuels' model as a function of elongation.

the nature of these functions, this model is valid up to an elongation of only about 50%. Thus, comparison of the patterns obtained with experimental results above this extension is not surprisingly different. To our knowledge, these are the first calculations of the scattering behavior for deformed spherulites having the 0–90° Hv pattern. While the data are of interest, the more fundamental question is just why is there a change in the polarizability axis within the spherulites with different thermal and solvent history. As yet, this question has not been answered, although it is being addressed.[23]

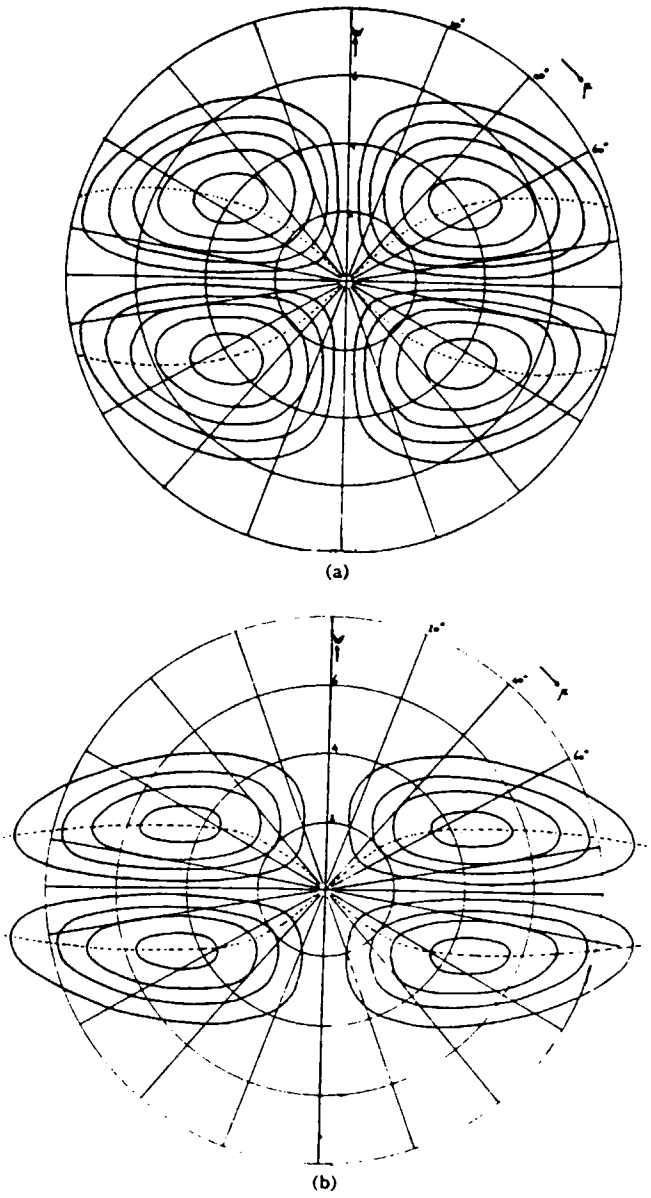

Fig. 20. Theoretically predicted changes in the H_v SALS patterns using the Stein–Clough–Van Aarsten model as a function of elongation.

CONCLUSIONS

(i) The samples under study show a distinct T_g (β relaxation) at about −40°C which arises from the poly(ethylene oxide-hydantoin) soft segment. For a given set of sample preparation conditions, there is no change in T_g with increase in the hard-segment content over the composition range studied.

(ii) At approximately −85°C, there is a lower temperature loss peak believed attributable to the secondary local-mode motions. This is apparently associated with the amorphous component of the hard segment.

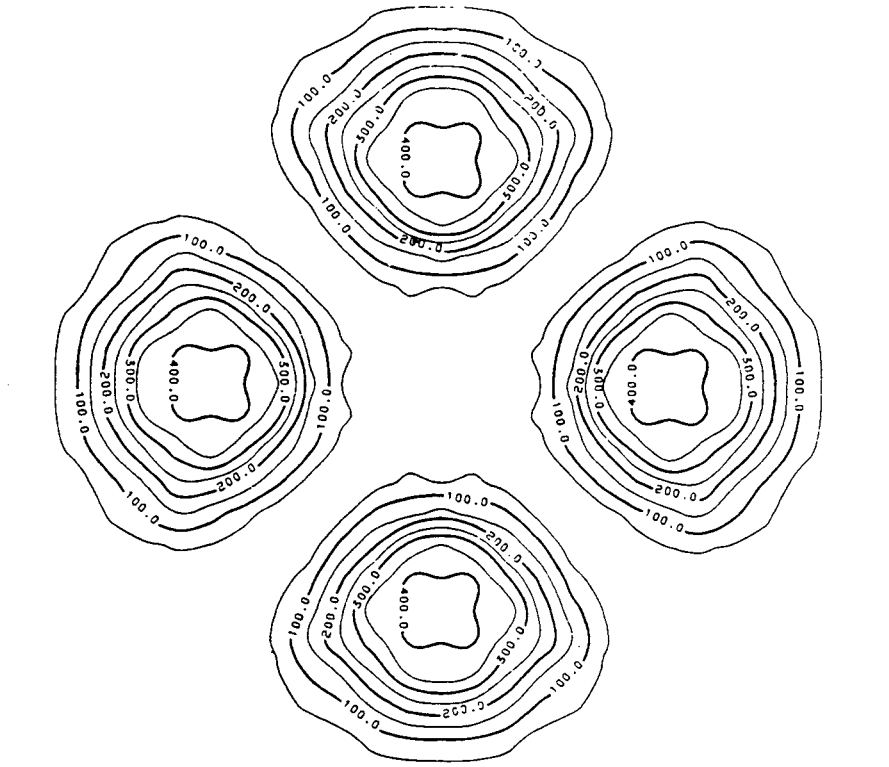

(a)

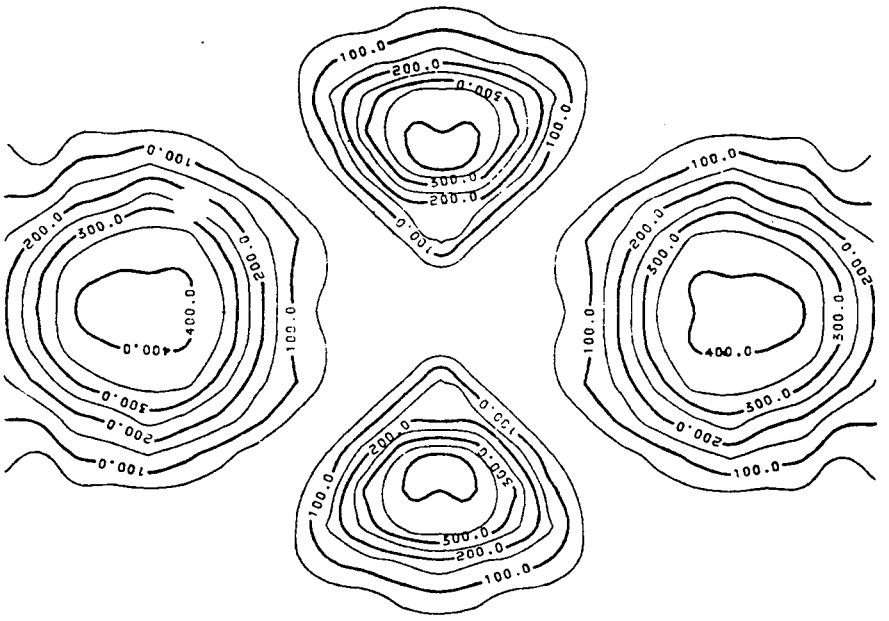

(b)

Fig. 21. Theoretically predicted H_v SALS patterns using Samuels' model at (a) $\lambda = 1.0$; (b) $\lambda = 1.5$; (c) $\lambda = 2.0$; (d) $\lambda = 3.0$.

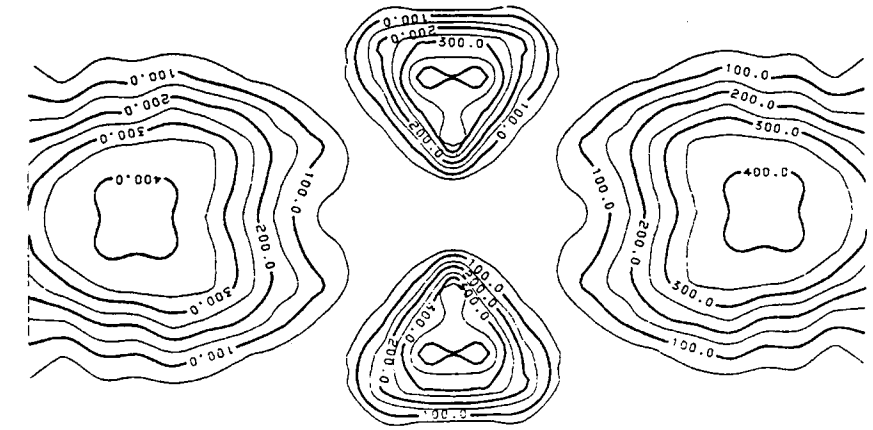

(c)

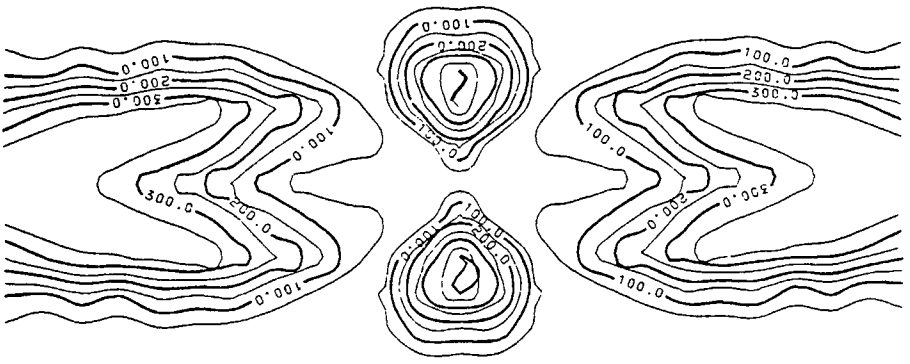

(d)

Fig. 21. (*Continued from previous page.*)

(iii) With an increase in the hard-segment content, the stress for a particular strain increases. Increasing the hard-segment content results in a higher modulus and a lower ultimate elongation. On annealing, some of the amorphous PBT segments crystallize, and consequently a higher value of stress is required for the same percent elongation.

(iv) Orientation measurements on these samples show that the orientation effect is primarily due to the PBT crystalline phase; but it is uncertain if there is a significant orientation effect due to the amorphous PBT phase and whether its contribution to the overall orientation function is significant. It can also be concluded that the orientation–disorientation process of the PBT segment is not instantaneous. No significant orientation was observed in the soft segment, although this may not be surprising due to its rubbery nature.

(v) The superstructure is clearly spherulitic in nature. On deformation, these spherulites tend toward ellipsoids.

(vi) Different film preparation conditions give different spherulitic morphology. Theoretical calculations for the so-called unusual 0–90° spherulites using Samuels' model give patterns which behave similarly to experimental

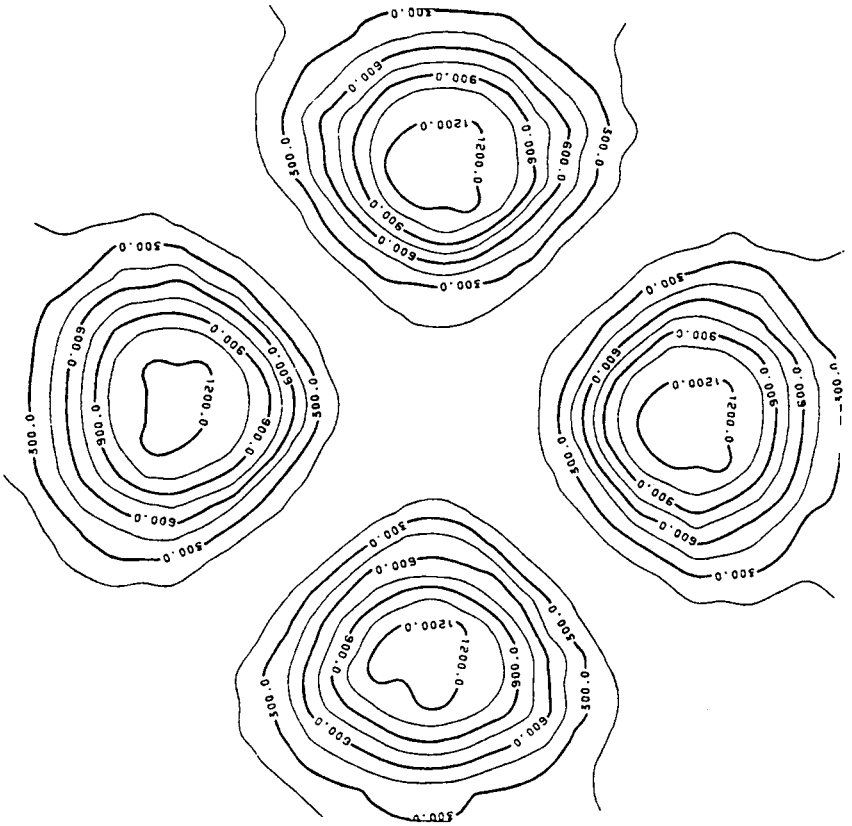

(a)

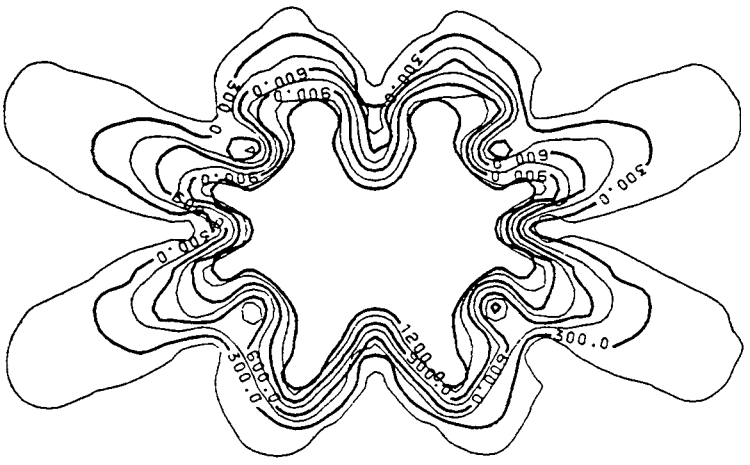

(b)

Fig. 22. Theoretically predicted Hv SALS patterns using the Stein–Clough–Van Aarsten model at (a) $\lambda = 1.0$; (b) $\lambda = 1.2$; (c) $\lambda = 1.5$.

observations. On the other hand, the Stein–Clough–Van Aartsen model does not give results similar to experimental observations.

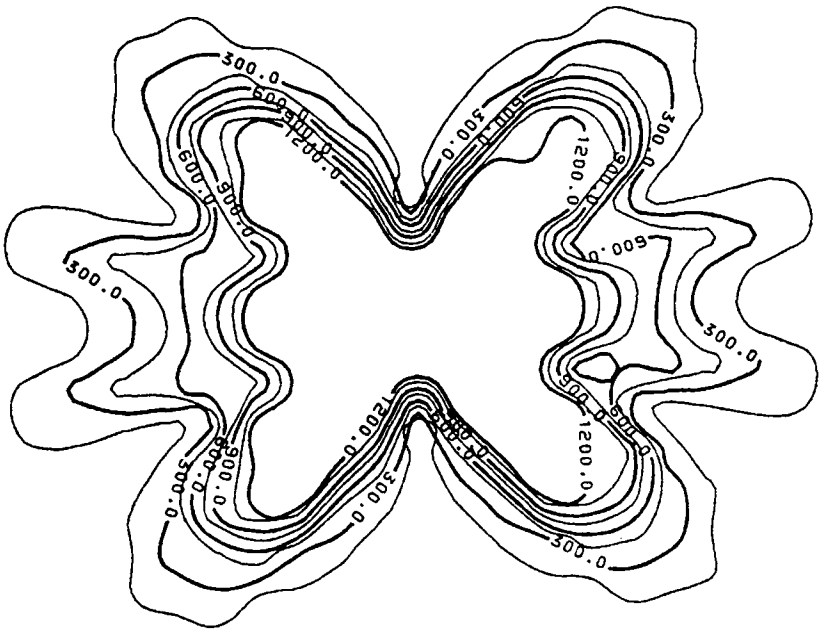

(c)

Fig. 22. (*Continued from previous page.*)

APPENDIX

Two models that exist by which one can predict light scattering patterns are (a) Samuels' model,[21] which is a three-dimensional approach; and (b) the Stein–Clough–Van Aartsen model,[22] which is a two-dimensional approach.

Samuels' Model

The equations by which one can predict the shape of a spherulite by its scattering of polarized light are

$$I_{H_v} = A\rho^2 V_o^2 \left(\frac{3}{U^3}\right)^2 \left[(\alpha_r - \alpha_t) \cdot \cos^2\frac{\theta}{2} \cdot \cos^2(\mu \pm \beta) \times \sin^2(\mu \pm \beta) \cdot (4\sin U - U\cos U - 3\,\mathrm{SiU})\right]^2 \quad \text{(A1)}$$

where I_{H_v} is the intensity of scattered light from H_v polarization, V_o is the volume of the anisotropic sphere, A is a proportionality constant, ρ is a geometric polarization correction term defined as

$$\rho = \cos\theta\,(\cos^2\theta + \sin^2\theta\,\sin^2\mu)^{-1/2} \quad \text{(A2)}$$

α_t and α_r are the tangential and radial polarizabilities of the anisotropic sphere. SiU is the sine integral defined by

$$SiU = \int_0^U \frac{\sin x}{x}\,dx \quad \text{(A3)}$$

and is solved as a series expansion sum for computational purposes. U is the shape factor and is defined as

$$U = \frac{4\pi R_o(\lambda s)^{1/2}}{\lambda} \sin\frac{\theta}{2}\left[1 + (\lambda_s^3 - 1)\cos^2\frac{\theta}{2}\cos^2\mu\right]^{1/2} \quad \text{(A4)}$$

where R_o is the radius of the spherulite, λ is the wavelength of light in the medium, λ_s is the principal extension ratio of a uniaxially deformed spherulite at constant volume, θ is the radical scattering angle, μ is the azimuthal scattering angle, and β is the angle which the principal polarizability axis

makes with the radial direction and is generally the angle at which the molecular chains are tilted to the lamellar surface, the lamellar principal axis lying in the radial direction.

In order to obtain the ±45° four clover leaf pattern, $\beta = 0$ in the above set of equations. This is for the case when the polarizability of the lamellae is either parallel or perpendicular to the radial direction. When the polarizability axis of the lamellae is inclined at 45° or the molecular chains are tilted at 45° to the lamellar surface (the lamellar principle axis being in the radial direction), $\beta = 45°$ and one obtains the 0–90° four clover leaf pattern. The final scattering intensity is obtained by adding intensities obtained from eq. (1) by putting $\beta = +45°$ and $\beta = -45°$.

Stein–Clough–Van Aartsen Model

The equations for this model are

$$I_{H_v} = (E_{H_v})^2$$

and

$$E_{H_v} = k^1(\alpha_1 - \alpha_2)Nc\frac{\lambda_2\lambda_3}{(\lambda_2^2 + \lambda_3^2)}A\frac{2}{X^2}\left(\left[1 + \left(\frac{1}{4}\right)F^2\right] \times \sin(2\gamma)[2 - 2J_0(X) - XJ_1(X)] + \left(\frac{1}{2}\right)F\sin(4\gamma)\left[-8 + 8J_0(X) + \left(X - \left(\frac{24}{X}\right)\right)J_1(X)\right] + \left(\frac{1}{8}\right)F^2\sin(6\gamma)\left[18 - 18J_0(X) - \left[X - \frac{144}{X}\right] \times J_1(X) - \left(\frac{480}{X^2}\right)J_2(X)\right] + \cdots\right) \quad \text{(A6)}$$

where $A = \pi R^2$, the area of the disc spherulite,

$$k = CE_0\cos^2\rho$$

where $\cos\rho = \cos\theta[\cos^2\theta + \sin^2\sigma\sin^2\mu]^{-1/2}$, C and E_0 are constants, α_1 and α_2 are the principal polarizabilities per unit area (which are assumed constant throughout the spherulite), N_c is the number of crystals per unit area, λ_2 is the extension ratio, $\lambda_3 = 1/\lambda_2$ (=0.5), $F = (\lambda_3^2 - \lambda_2^2)/(\lambda_3^2 + \lambda_2^2)$, and

$$X = rR\sin\theta\,[\lambda_2^2\sin^2(\mu \pm \beta) + \lambda_3^2\cos^2(\mu \pm \beta)]^{1/2}$$

$$= \sin^{-1}\frac{\lambda_2\sin\mu}{(\lambda_2^2\sin^2\mu + \lambda_3^2\cos^2\mu)^{1/2}}$$

where σ and μ are the radial and azimuthal angles respectively, and β is the angle as defined earlier in Samuels' model.

To obtain the ±45° four clover-leaf type of pattern, $\beta = 0$ in the above set of equations. For $\beta = \pm 45°$, the patterns obtained as a function of extension do not behave similarly to the experimental results.

References

1. R. J. Cella, *J. Polym. Sci. Symp.*, **No. 42**, 727 (1973).
2. J. R. Wolfe, Jr., *Rubber Chem. Technol.* **50**(4), Sept.–Oct. (1977).
3. A. Lilanitkul and S. L. Cooper, *Rubber Chem. Technol.*, **50**(1), March–April (1977).
4. S. L. Samuels and G. L. Wilkes, *J. Polym. Sci., Part C*, **43**, 149 (1973).
5. A. E. Allegrezza, Jr., R. W. Seymour, N. N. Ng, and S. L. Cooper, *Polymer*, **15**, 433 (1974).
6. I. Kimura, H. Ighihara, M. Ono, N. Yochihara, S. Nomura, and H. Kawai, *Macromolecules*, **1**, 355 (1974).
7. M. Shen, U. Mehra, M. Nieinomi, J. K. Koberstein, and S. L. Cooper, *J. Appl. Phys.*, **45**(10), 4182.
8. R. W. Seymour, J. R. Overton, and L. S. Corley, *Macromolecules*, **8**, 331 (1975).
9. A. Lilamitkul, J. C. West, and S. L. Cooper, *J. Macromol. Sci. Phys.* **12**(4), 563 (1976).
10. A. Lilamitkul, G. M. Estes, and S. L. Cooper, *Polym. Prep. Am. Chem. Soc. Div. Polym. Chem.*, **18**(2), 500 (1977).
11. G. L. Wilkes, *J. Macromol. Sci.*, Rev. Macromol. Chem., **C10**(2), 149 (1974).
12. S. Abouzahr, G. L. Wilkes, and Z. Ophir, manuscript in preparation.

13. G. Farrow, T. McIntoch, and I. M. Ward, *Makromol. Chem.*, **38**, 147 (1960).
14. K. H. Illers and B. Brown, *J. Colloid Sci.*, **18**, 1 (1963).
15. C. S. Paik Sung, T. W. Smith, C. B. Hu, and Nak-Ho Sung, *Macromolecules*, to appear.
16. L. R. G. Treloar, *The Physics of Rubber Elasticity*, 2nd ed., Oxford University Press, London, 1958.
17. M. C. Tobin, *J. Phys. Chem.*, **61**, 1392 (1957).
18. C. Y. Liang and S. Krimm, *J. Mol. Spect.*, **3**, 554 (1959).
19. I. M. Ward and M. A. Wilding, *Polymer*, **18**, 327 (1977).
20. R. J. Samuels, Crystal and Wilkes.
21. R. S. Samuels, *Structured Polymer Properties*, Wiley–Interscience, New York, 1974.
22. S. Clough, J. J. Van Aartsen, and R. S. Stein, **36**(10), 3072 (1965).
23. R. S. Stein, private communication.

Received October 10, 1980
Accepted February 11, 1981